First-principles study on thermal expansion of W-Re sigma and chi phases

Vesti, Anders; Music, Denis; Olsson, Pär

Published in:
Nuclear Materials and Energy

DOI:
10.1016/j.nme.2024.101684

2024

Document Version:
Publisher's PDF, also known as Version of record

Nuclear Materials and Energy 39 (2024) 101684

Contents lists available at ScienceDirect

Nuclear Materials and Energy

journal homepage: www.elsevier.com/locate/nme

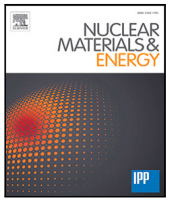

First-principles study on thermal expansion of W-Re sigma and chi phases

Anders Vesti [a,*], Denis Music [b,c], Pär A.T. Olsson [a,b]

[a] Division of Mechanics, Materials & Component Design, Department of Mechanical Engineering Sciences, Lund University, Box 118, SE-221 00 Lund, Sweden
[b] Materials Science and Applied Mathematics, Malmö University, SE-205 06 Malmö, Sweden
[c] Biofilms Research Center for Biointerfaces, Malmö University, SE-205 06 Malmö, Sweden

ARTICLE INFO

Keywords:
Tungsten
Rhenium
DFT
Thermal expansion
σ
χ
Precipitates

ABSTRACT

We investigate how the Re content affects the coefficient of thermal expansion (CTE) of the non-stoichiometric W-based σ and χ phases, forming upon neutron irradiation of W, to explore and quantify its mismatch between precipitates (W-Re) and matrix (W). To this end, we have conducted first-principles calculations using two approaches: the Debye-Grüneisen (DG) model and the quasi-harmonic approximation (QHA). The two approaches yield different results: the QHA, which is deemed to be the most accurate of the two, predicts substantial changes with Re content, while the acoustic-modes based DG model does not. The CTE of the σ and χ at stable Re contents is compared to experimental values for bcc-W and bcc-W-Re containing 25 at.% Re. Taking bcc-W as a reference, we find a significant mismatch in CTE of up to 37% and 62% for σ and χ, respectively, which may contribute to thermal stress buildup in the material at elevated temperatures. The mismatch is shown to increase with the temperature and Re content for both phases. The produced data are used to fit a temperature and Re concentration-dependent analytical function of the CTE for both phases, which can be employed as input for continuum mechanical modeling.

1. Introduction

Tungsten (W) and its alloys are highly attractive as the basis of plasma-facing components (PFC) in fusion reactors due to advantageous properties such as high thermal conductivity, high melting point, and low sputtering yield [1,2]. The W-based PFCs have been tested in multiple experimental reactors [3,4], the ITER reactor will feature a W-based divertor [5,6], and such development is underway also for the Wendelstein 7-X test reactor [7]. Furthermore, W-based components are expected to be critical for the proposed demonstration fusion power plants like DEMO [2,8]. A major concern in developing PFCs is the response of the components to the harsh operating environment with plasma exposure, high thermal loads, and high flux neutron irradiation [9–12]. Especially the neutron irradiation will cause microstructural changes in the material. The formation of σ and χ precipitates consisting of W and its transmutation product, rhenium (Re), is one example of such changes [13–17]. Due to neutron irradiation-induced precipitation [18,19], they have been shown to form at overall Re concentrations far below the solubility limit [20]. How these precipitates may affect the longevity and structural stability of the W-based components under the harsh operating environment is not yet fully understood [4].

In previous studies, *ab-initio* tools, such as density functional theory (DFT), have been used to explore the properties of the W-Re σ and χ phases, such as the lattice site occupancy [21,22] along with elastic and fracture-related properties [23,24]. However, an important property currently overlooked in the literature is the coefficient of thermal expansion (CTE). A mismatch in CTE between the host matrix and a precipitate leads to a buildup of thermal stresses, which may cause the initiation and propagation of cracks as well as the generation of dislocations. Such dislocations can interact with the σ and χ precipitates thereby affecting the mechanical properties of the W-based alloy, such as the hardness and brittleness [25,26]. Since PFCs are subjected to large temperature fluctuations and cyclic thermal gradients during reactor operation, a significant mismatch in CTE could reduce the service lifetime of the components due to thermal fatigue. Experiments reveal a high mismatch in CTE of up 50% between hcp-Re [27] and bcc-W [28] at the high temperatures at which ITER will operate [9]. Additionally, both experiments and simulation studies show that increasing Re content in bcc-W generally causes an increase in the CTE [29–31], with DFT calculations predicting a 38%–40% increase in CTE of bcc-W containing 50 at.% Re at 1000–1400 K [32], whereby σ and χ remain unexplored. This raises concerns for the high Re-content σ and χ precipitates, especially the χ phase, which can contain up to 75 at.% Re according to the phase diagram [20].

In the present work, we estimate the CTE using DFT and apply two common approaches for thermal expansion: the Debye-Grüneisen (DG)

* Corresponding author.
E-mail address: anders.vesti@lth.lu.se (A. Vesti).

https://doi.org/10.1016/j.nme.2024.101684
Received 11 April 2024; Received in revised form 23 May 2024; Accepted 28 May 2024
Available online 29 May 2024

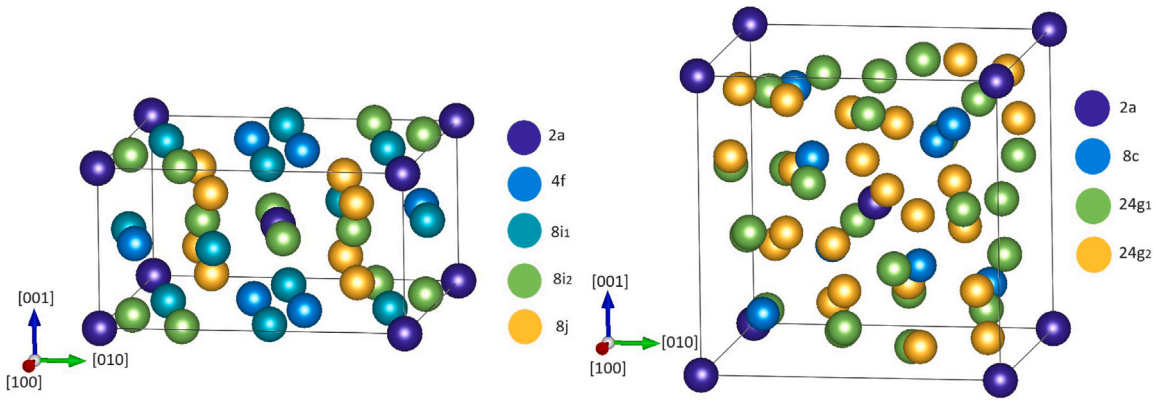

(a) Tetragonal unit cell of σ (b) Cubic unit cell of χ

Fig. 1. Unit cells of the (a) σ and (b) χ phases. Atomic positions have been colored with respect to their Wyckoff sites. The unit cells are created using VESTA [36].

model [33] and quasi-harmonic approximation (QHA) [34], as there is a lack of experimental data. These approaches have their advantages and disadvantages. The DG model is attractive because it is computationally fast since the phonon density of states (PDOS) is approximated rather than explicitly calculated. The QHA, on the other hand, is based on *ab-initio* calculation of the PDOS making it more accurate but also computationally expensive. The calculations are performed on several σ and χ supercells with varying Re content. A unique challenge for the σ and χ phases is that they are stable over a range of Re concentrations. Therefore, it is of interest to determine the CTE as a function of the Re concentration as well as temperature. To accomplish this, we adopt a framework inspired by the sublattice method which has previously been applied to the σ and χ phases [22,23,35]. In this framework, the non-equivalent lattice sites, also known as the Wyckoff sites, are treated as sublattices. The formation enthalpy of every possible sublattice configuration is then determined. This allows us to focus our study to the most stable sublattice configurations of σ and χ.

We find that the DG and QHA result in opposite trends of the Re dependence of the CTE. This difference is interpreted by analyzing how the methods treat the PDOS. We argue that the DG model is less appropriate for the σ and χ because it only considers acoustic phonon modes. From the QHA results of the most stable sublattice configurations, we provide an analytical function of the thermal expansion for σ and χ as a function of Re content and temperature. This can be used as input for future continuum mechanical modeling of matrix-precipitate interaction at elevated temperatures. From analysis of the PDOS, we further find that the σ-phase is not dynamically stable at high Re concentrations. Lastly, we estimate the mismatch in CTE between σ and χ precipitates and the surrounding bcc matrix by comparing our results with experimental data from the literature for bcc-W and W-Re with Re contents near the solubility limit. We find that both types of precipitates show significant values of mismatch in CTE at high temperatures with the χ phase expected to have the largest mismatch. Further studies of the consequences of the large CTE mismatch are justified as the results may negatively affect the longevity of the W-based component.

2. Method

2.1. The σ and χ-phase

The σ-phase has a tetragonal crystal structure and belongs to the space-group $P4_2/mnm$, while the χ-phase exhibits a cubic symmetry with the $I\bar{4}3m$ space-group [22]. The unit cell of σ contains 30 atoms located at five Wyckoff sites: $2a$, $4f$, $8i_1$, $8i_2$, and $8j_2$, while the cubic unit cell of χ comprises of 58 atoms distributed among four Wyckoff sites: $2a$, $8c$, $24g_1$, and $24g_2$, see Fig. 1. Both phases are thermodynamically stable over a range of Re concentrations as seen in the W-Re phase diagram [20] and have no fixed stoichiometry. An efficient way to treat this disorder is by applying the sublattice method as described in the literature [35]. In this approach, the aforementioned Wyckoff sites are treated as sublattices occupied by either W or Re. By adopting this approach, several σ and χ configurations of different Re concentrations were created. The formation enthalpy of the configurations was calculated by subtracting the energies of W and Re in their reference states ($E_W^{bcc} = -12.9507$ eV/at. and $E_{Re}^{hcp} = -12.4259$ eV/at.) from the energy per atom of the σ and χ states

$$H_f^{\sigma} = E_{klmno}^{\sigma} - x_W \cdot E_W^{BCC} - x_{Re} \cdot E_{Re}^{HCP},$$
$$H_f^{\chi} = E_{klmn}^{\chi} - x_W \cdot E_W^{BCC} - x_{Re} \cdot E_{Re}^{HCP}, \quad (1)$$

where the subscript, $klmn(o)$, refers to the occupancy of the Wyckoff sites of the configurations and x_i is the atomic fraction of W (or Re) in the configuration. We limited our study to the most stable sublattice configurations on the convex hull.

2.2. Coefficient of thermal expansion

The volumetric CTE is given by

$$\alpha_V = \frac{1}{V}\frac{\mathrm{d}V}{\mathrm{d}T}, \quad (2)$$

where V is the volume and T is the temperature. In the lack of experimental data, α_V can be estimated using computational methods in which the temperature-dependent equilibrium volume is determined from the Helmholtz free energy, which can be expressed as

$$F(V,T) = E_0(V) + F_{vib}(V,T) + F_{el}(V,T) \quad (3)$$

where $E_0(V)$ is the strain energy of the ground state and $F_{vib}(V,T)$ is the vibrational free energy. $F_{el}(V,T)$ is the free energy contribution due to electronic excitations [37] which consists of two terms: $F_{el} = E_{el} - T \cdot S_{el}$ where

$$E_{el}(T,V) = \int_{-\infty}^{\infty} n(\varepsilon,V)\, f(\varepsilon,T)\varepsilon d\varepsilon - \int_{-\infty}^{\varepsilon_F} n(\varepsilon,V)\,\varepsilon d\varepsilon \quad (4)$$

and

$$S_{el}(T,V) = -k_B \int_{-\infty}^{\infty} n(\varepsilon,V)\,[f(\varepsilon,T)\ln f(\varepsilon,T) + \cdots$$
$$(1-f(\varepsilon,T))\ln(1-f(\varepsilon,T))]d\varepsilon \quad (5)$$

here ε is the energy level, ε_F is the Fermi energy, $n(\varepsilon,V)$ is the electron density of states, and $f(\varepsilon,T)$ is the Fermi-Dirac distribution. The two terms were calculated using the method as described elsewhere [38].

Within the DG formalism, the vibrational free energy term can be specified as

$$F_{vib}^{DG} = -nk_B T\left[3\left(\frac{T}{\Theta}\right)^3\int_0^{\Theta/T}\frac{x^3}{e^x-1}dx - 3\ln\left(1-e^{-\frac{\Theta}{T}}\right) - \frac{9\Theta}{8T}\right] \quad (6)$$

with k_B being the Boltzmann constant, n being the number of atoms, and Θ the Debye temperature [39]. By applying the Slater approximation [40], the Grüneisen parameter, γ, was estimated as

$$\gamma = -\frac{2}{3} - \frac{V}{2}\frac{\partial^2 P/\partial V^2}{\partial P/\partial V}, \quad (7)$$

where P is the static lattice pressure at 0 K [33]. As a first approximation, γ can be assumed to be volume-independent [41] and Eq. (7) was evaluated at the equilibrium volume V_0. The volume dependency of Θ, as introduced by Moruzzi et al. [41], was utilized via

$$\Theta\left(V, V_0\right) = \Theta_0\left[\frac{V_0}{V}\right]^{\gamma}, \quad (8)$$

where the Debye temperature evaluated at the equilibrium volume, Θ_0, was estimated using the elastic constants of the structures [33]. The elastic constants of σ were adopted from [23], while those of χ were adopted from our earlier work [24].

In the QHA, the vibrational free energy is calculated from the PDOS via the expression

$$F_{vib}^{QHA}(T,V) = \frac{1}{2}\int_0^{\infty} g(\omega,V)\,\hbar\omega d\omega + \cdots \\ k_B T\int_0^{\infty} g(\omega,V)\ln\left[1-\exp\left(-\frac{\hbar\omega}{k_B T}\right)\right]d\omega \quad (9)$$

where ω is the phonon frequency, $g(\omega, V)$ is the PDOS, and $\hbar$ is the reduced Planck constant [34].

Helmholtz free energy, $F(V,T)$, was calculated for 11 volumes by applying equally spaced strain increments in the range −1% to 1%, such that a hydrostatic stress state was obtained. For the non-cubic σ-phase, the ratio of the strain in the x_1- and x_2-direction, and that in the x_3-direction, was computed by applying a hydrostatic stress to the compliance matrix. In general, for tetragonal crystals the applied strain corresponds to $\varepsilon_{11} = \varepsilon_{22} \neq \varepsilon_{33}$, with the relation between strains being

$$\frac{\varepsilon_{11}}{\varepsilon_{33}} = \frac{C_{33}-C_{13}}{C_{11}+C_{12}-2C_{13}}, \quad (10)$$

which was computed using the elastic constants at $T = 0$ K from [23,24]. For the cubic χ-phase, this relation boils down to $\varepsilon_{11} = \varepsilon_{22} = \varepsilon_{33}$. The free energy-volume data were fitted to the Birch–Murnaghan equation of state to obtain the temperature-dependent equilibrium volume [42]. The isothermal bulk modulus, B, can readily be obtained from the Birch–Murnaghan equation of state. The volumetric thermal expansion was calculated by numerical differentiation of the temperature-dependent equilibrium volume.

2.3. Dependency of α_V on the Re content

To estimate the thermal expansion as a function of Re content and T, the CTEs of the sublattice configurations were utilized as reference data to fit an analytical function using the linear least-squares fitting method with Trust-Region regularization [43]. The function of $\alpha_v(x_{Re}, T)$, was written as a separable-function

$$\alpha_V(x_{Re}, T) = \Psi(x_{Re})\cdot\Phi(T), \quad (11)$$

where $\Psi(x_{Re})$ determines the Re content dependency. The form was chosen as the sum of two exponential functions which provided a good fit

$$\Psi(x_{Re}) = \sum_{i=1}^{2} a_i \exp\left(b_i x_{Re}\right), \quad (12)$$

where a_i, and b_i are fitting parameters. For the temperature dependency, we adopted a recently developed equation of state for W [44]

$$\Phi(T) = \sum_{i=1}^{3}\frac{X_i\Theta_i^2\exp\Theta_i/T}{T^2\left(\exp\Theta_i/T-1\right)^2} + gkT^{k-1} \quad (13)$$

with X_i, Θ_i, g and k being fitting parameters. The function comprises a three-term Einstein function plus an additional anharmonic term. We note that a similar expression has been used to describe the thermal expansion of several refractory metals including W [28,44].

2.4. Computational details

For the DFT calculations, the Vienna *Ab initio* Simulation Package (VASP 5.4) was used [45,46] with projector augmented wave (PAW) potentials for W and Re with valence configurations of $5s^2 5p^6 6s^1 5d^5$ and $6s^1 5d^6$ [47,48], respectively. The generalized gradient approximation based on the Perdew–Burke–Ernzerhof exchange–correlation functional [49] was adopted and the Methfessel–Paxton method [50] for smearing with a width of 0.1 eV was applied. The Monkhorst–Pack scheme [51] was used to generate Γ-centered k-point grids. Convergence tests revealed that a cut-off energy of 650 eV and k-point grids of 7 × 7 × 13 and 7 × 7 × 7 were sufficient for the σ and χ unit cells. When treating supercells, the k-point grid was adjusted appropriately. A quasi-Newton algorithm [52] was used for ionic relaxation with a strict force convergence criterion of 0.1 meV/∀, which was necessary to produce well-converged phonon data. Calculations were also carried out on bcc-W and hcp-Re unit cells utilizing a cut-off energy of 450 eV and grids of 18 × 18 × 18 and 15 × 15 × 8 k-points. The relaxed unit cell parameters were in good agreement with experiments with deviation of less than 1%, that is for bcc-W: a_0 = 3.185 ∀ (expt. 3.155 ∀ [53]) and for hcp-Re a_0 = 2.771 ∀ and c_0 = 4.490 ∀ (expt. 2.761 ∀ and 4.456 ∀ [54], respectively).

The QHA calculations were carried out using *Phonopy* [55–57] in which a variant of the Parlinski–Li–Kawazoe method [58,59] is employed to obtain the force constants needed to compute the phonon dispersion and PDOS. The integration over the PDOS was performed on 39 × 39 × 61 and 39 × 39 × 39 q-point meshes for σ and χ structures respectively. To ensure that all relevant contributions to the force constants were included, convergence tests of the supercell size were performed. For the σ phase supercells of sizes 1 × 1 × 2, 1 × 1 × 3, and 1 × 1 × 4 times the unit cell were tested. We found that a supercell of size 1 × 1 × 2 gave converged results with a difference in CTE of less than 0.6% at 1000 K compared to the 1 × 1 × 3 supercell. The cubic χ unit cells, which have approximately twice the volume of the σ unit cell and the lattice parameter of ∼ 10 Å, were deemed large enough for convergence (see Table A.1). For bcc-W, a supercell of 4 × 4 × 4 times the cubic unit cell, and for hcp-Re a supercell of 5 × 5 × 3 times the hexagonal unit cell gave converged results. The integration over the PDOS was carried out on 45 × 45 × 45 and 85 × 85 × 45 q-point meshes for bcc-W and hcp-Re respectively.

3. Results

In Fig. 2 the formation enthalpy at 0 K of the σ and χ sublattice configurations are plotted against the Re content. The convex hull is drawn for σ and χ using the common tangent method to connect the most stable configurations. The sublattice configurations investigated in this work have been numbered and a table with the basic properties of the structures is provided in the appendix (see Table A.1). The configurations of the lowest formation enthalpy occur when Re atoms occupy the low coordination number Wyckoff sites, that is σ No. 9 (H_f^{σ} = 0.028 eV/atom), and χ No. 13 (H_f^{χ} = −0.008 eV/atom). These configurations have Re content equal to the ideal compositions of the phases: σ-W_2Re and χ-W_5Re_{24}. The preference of Re for the sites of low coordination number agrees with the findings of other investigations [21,60]. While the σ configurations no. 6 and no. 26 are

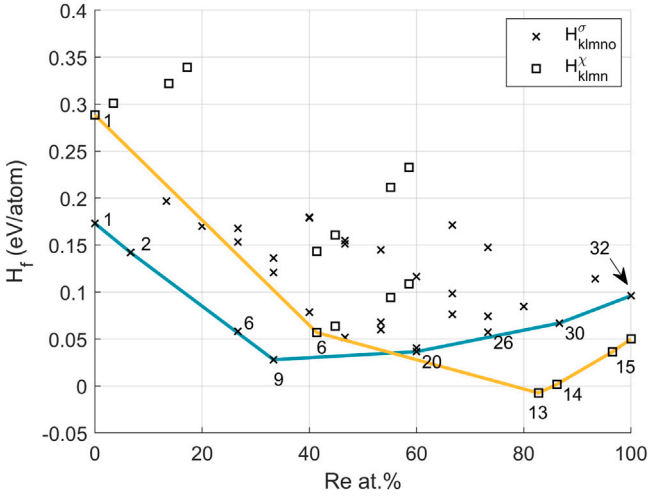

Fig. 2. Formation enthalpies of the sublattice configurations for σ and χ. Common-tangent lines between the most stable configurations are drawn forming a convex hull. The selected configurations have been numbered according to Table A.1.

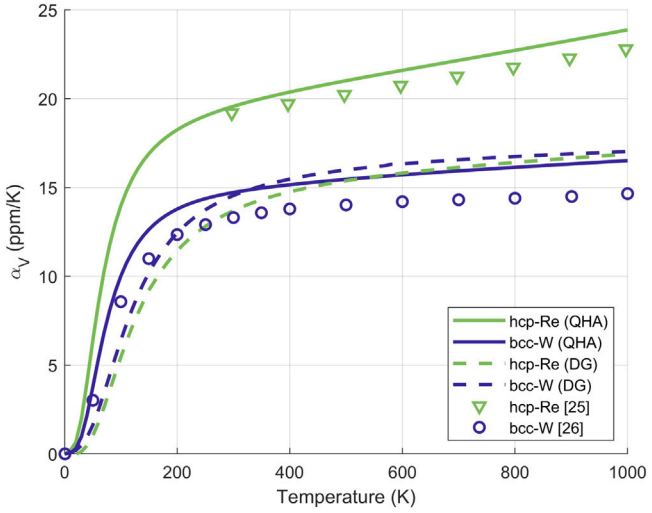

Fig. 3. The volume CTE for bcc-W and hcp-Re. Solid lines indicate QHA results while dashed lines indicate DG results. Experimental data are shown with symbols [27,28].

not part of the convex hull, they were included due to their proximity. The σ configurations of high Re concentrations: no. 26 (73 at.%), no. 30 (87 at.%) and no. 32 (100 at.%) were found to be dynamically unstable due to imaginary frequencies observed in the PDOS and the CTE of these configurations could therefore not be obtained.

To benchmark our implementation, QHA and DG results for α_V and the isothermal bulk modulus, B, were compared with experimental data for bcc-W and hcp-Re in Fig. 3 and Fig. 4 respectively. In Fig. 3 it can be seen that the QHA results, plotted with a solid line, show good agreement with experiments: at 1000 K, where the deviation is largest, QHA predicts values of α_V that are 13% and 5% higher than experiments for bcc-W and hcp-Re, respectively. Even though the DG model predicts values of α_V for bcc-W that are close to experiments, it greatly underestimates the values for hcp-Re. Others have observed similar discrepancies [64,65]. It has been suggested to be due to the inherent limitation of the DG model itself, which does not include the contribution of the optical phonon modes [65]. Another issue is that the estimation of γ within the DG method is critical [66] leading to possible discrepancies.

The isothermal bulk modulus, B, is shown in Fig. 4. Comparison with experimental values shows again good agreement: at 1000 K,

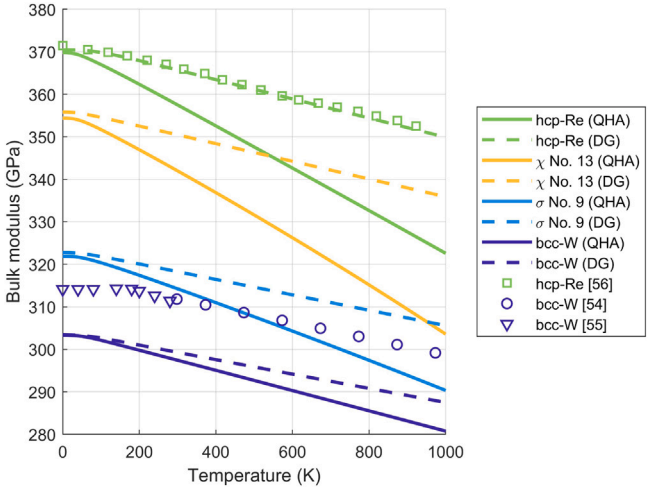

Fig. 4. Bulk modulus as a function of temperature for bcc-W, hcp-Re and the most stable σ and χ sublattice configurations. Experimental data are shown as symbols [61–63].

the deviations of the QHA are 6% and 8% for bcc-W and hcp-Re, respectively. The DG method's deviations are smaller still since it more accurately reproduces the slopes of $B(T)$. However, it should be noted that because resonance-based experiments resemble adiabatic conditions, isentropic B would be a more accurate comparison [67]. Because the isothermal B is a lower limit of the isentropic values [67], the direct comparison between DFT and experimental data is somewhat misleading and would suggest that the QHA is in fact in closer agreement with experimental data than Fig. 4 reveals.

Results for σ No. 9 and χ No. 13 are also shown in Fig. 4. For σ No. 9 the bulk modulus is 322 GPa at 0 K and according to QHA decreases by 10% to 290 GPa at 1000 K while the DG model predicts a 6% decrease to 305 GPa. The modulus of χ-phase No. 13 is 354 GPa at 0 K and decreases by 14% to 304 GPa at 1000 K according to the QHA, versus a 6% decrease to 336 GPa as predicted by the DG model. The behavior of the bulk modulus of σ and χ follows the behavior of the Varshni relation [68] for the temperature dependence of the elastic properties

$$B(T) = B_0 - \frac{s}{\exp(t/T) - 1} \tag{14}$$

where B_0 is the bulk modulus at 0 K while s and t are material specific constants. In the Appendix, we provide fitted values of B_0, s and t for the 10 selected σ and χ configurations, see Table A.2.

In Fig. 5 the CTEs of the σ and χ sublattice configurations are shown. The QHA results are plotted with solid lines while the results of the DG are plotted with dashed lines. The configuration numbers and Re content are written in the figure legend. It is noticeable that the two approaches predict different Re dependence. Where the results of the DG model give rise to a minute change, the QHA predicts a trend of increasing α_V with increasing Re content. For example, at 1000 K the QHA method predicts a 12% increase in α_V between σ No. 1 and No. 20. For the χ phase, the QHA predicts a negligible difference between No. 1 (0 at.% Re) and No. 6 (41 at.% Re) but as the Re content increases further, the CTE of No. 15 (97 at.% Re) reaches 30.0 ppm/K at 1000 K, which is 45% higher than No. 1. Furthermore, at high Re content, the gradient of the α_V curves are steeper indicating a higher sensitivity of α_V to temperature fluctuations.

To further investigate the different predictions on the Re content dependency, we compare the Grüneisen parameter as obtained by the two approaches. The Grüneisen parameter is related to α_V according to the following relation [69]:

$$\alpha_V \sim \frac{\gamma}{BV}. \tag{15}$$

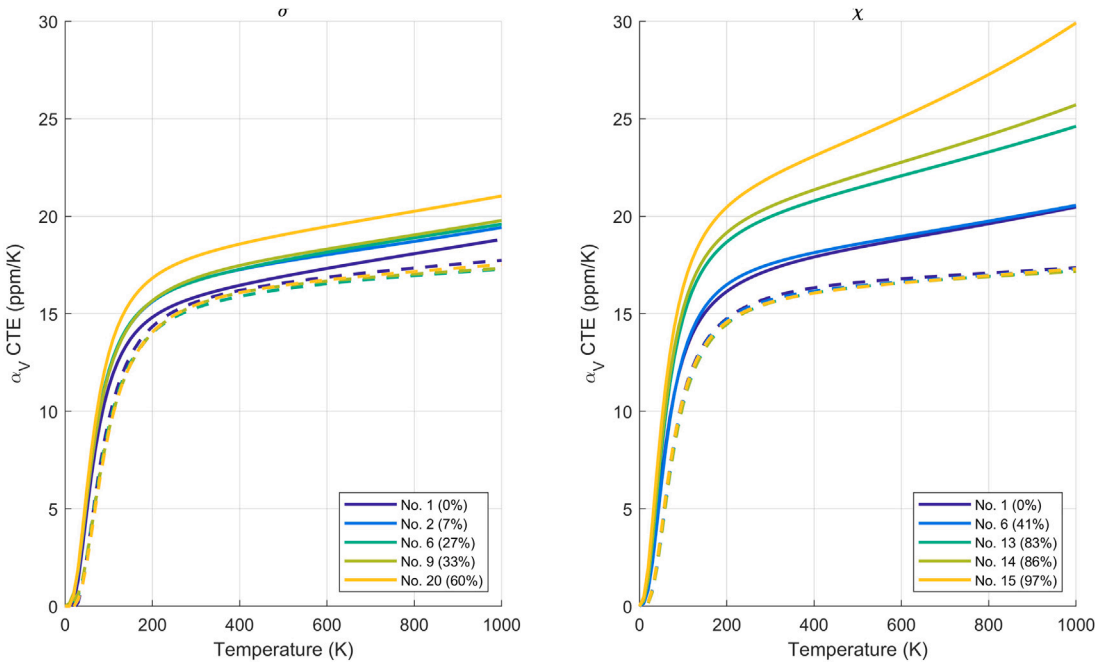

Fig. 5. The volume thermal expansion coefficient α_V for (a) σ and (b) χ sublattice configurations as predicted by QHA (solid line) and DG (dashed line). The legend indicates the sublattice No. and the atomic percentage of Re of the configurations.

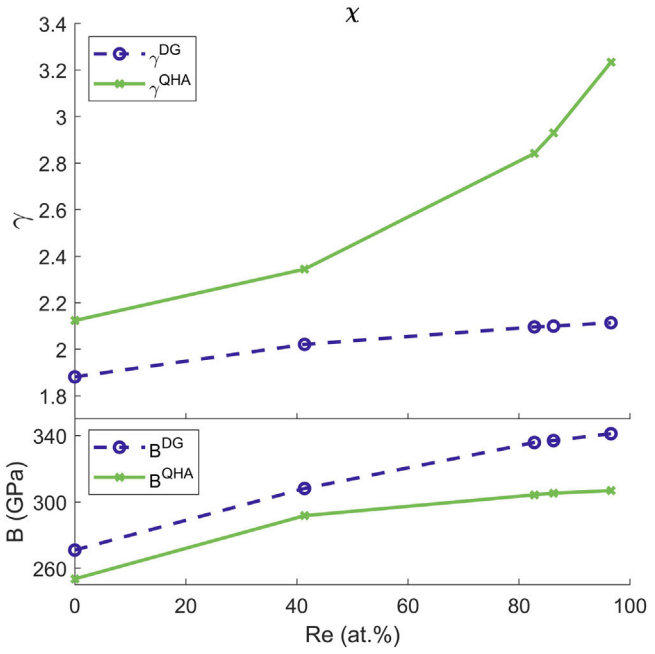

Fig. 6. The Grüneisen parameter (top panel) and the bulk modulus (bottom panel) at 1000 K of the χ sublattice configurations as obtained by the DG model and the QHA.

We find that the DG model and the QHA predict different trends of γ concerning the Re content, as seen for the χ phase in Fig. 6, where γ evaluated at 1000 K is shown in the top panel. The DG model yields a small nearly linear increase in γ that is counter-balanced by the rise in B when the Re content is increased, see bottom panel of Fig. 6, leading to a negligible change in α_V. The QHA, however, predicts a larger non-linear increase in γ, meaning that the most significant changes are observed at high Re contents. This explains why the difference in α_V of sublattice configurations No. 1 and No. 6 is negligible while the difference between configurations No. 13 and No. 14 is more pronounced despite the relatively small increase in Re content.

Table 1
Parameters of the function of $\alpha_V(x_{Re}, T)$ given in Eq. (11).

Parameter	σ	χ
X_1, (K^{-1})	$2.348 \cdot 10^{-7}$	$3.061 \cdot 10^{-7}$
X_2, (K^{-1})	$3.629 \cdot 10^{-7}$	$3.066 \cdot 10^{-7}$
X_3, (K^{-1})	$3.409 \cdot 10^{-8}$	$-1.717 \cdot 10^{-9}$
Θ_1, (K)	128.9	114.5
Θ_2, (K)	260.9	270.5
Θ_3, (K)	2150	2150
g, (K^{-k})	$8.944 \cdot 10^{-13}$	$5.929 \cdot 10^{-13}$
k	2.503	2.667
a_1	26.62	27.21
b_1	0.1918	−0.1239
a_2	0.6144	0.4879
b_2	$1.136 \cdot 10^{-2}$	3.400
RMSE, (ppm/K)	0.2419	0.3883

The σ phase contains a total of 90 phonon modes (3 acoustic modes and 87 optical modes) while the χ phase contains 87 modes (3 acoustic and 84 optical). In Fig. 7 the phonon dispersion structures of σ No. 9 and χ No. 13, are shown. The σ phase becomes dynamically unstable at high Re content as imaginary phonon modes are observed. Similar instabilities were found for the Cr-Re σ phase [70]. To the best of our knowledge, this is the first time the phonon dispersion of χ is shown. In both phases, the majority of the optical modes are located at a densely packed belt in the frequency range of 2–6 THz. This results in a complicated PDOS containing multiple sharp peaks arising from a broad background with no obvious gaps, as also seen in Fig. 7.

To determine the Re content dependency of the thermal expansion coefficient of σ and χ, Eq. (11) is fitted to the $\alpha_V(T)$ of the selected sublattice configurations of each phase located on the convex hull. Because the DG model predicts no significant Re dependency, the QHA results were used as reference data to perform the fit. The values of the fitting parameters are listed in Table 1. We obtain RMSE values of 0.2419 and 0.3883 ppm/K for σ and χ respectively, which at 1000 K equates to a deviation of a few percent. For the σ phase, $\alpha_V(x_{Re}, T)$ were only fitted within the stable Re concentration range. We discourage the use of the function outside of this Re range, as $\alpha_V(x_{Re}, T)$ increases

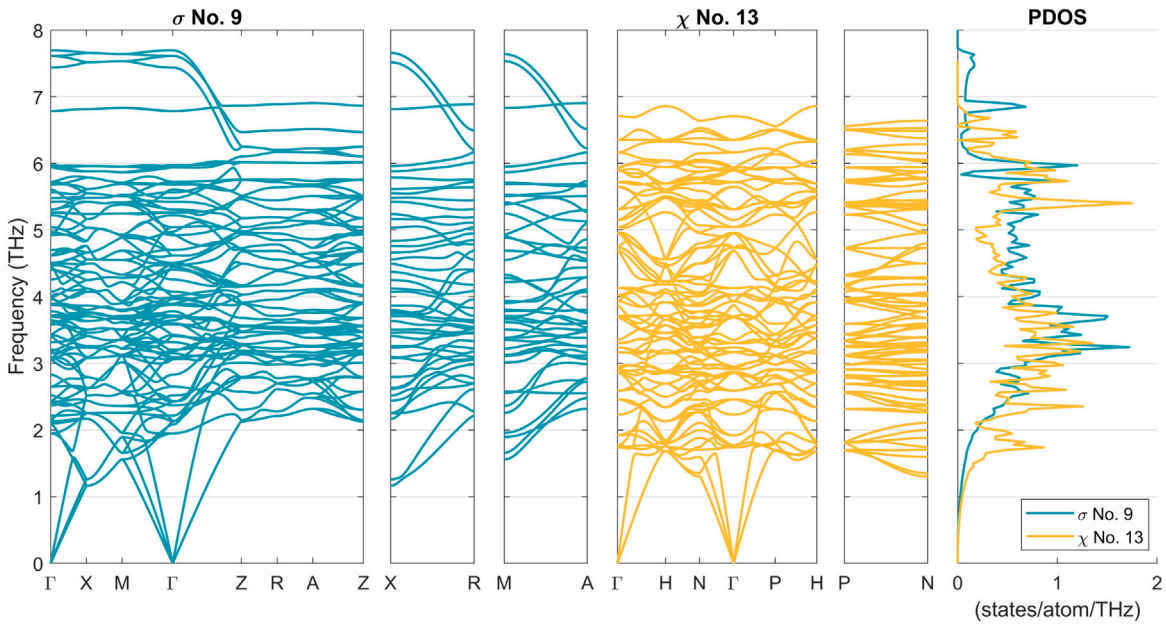

Fig. 7. The phonon dispersion of (a) σ No. 9 and (b) χ No. 13. The points of high symmetry are $\Gamma = (0,0,0)$, $X = (1/2,0,0)$, $Z = (0,0,1/2)$, $M = (1/2,1/2,0)$, $A = (1/2,1/2,1/2)$, $R = (0,1/2,1/2)$, $H = (1/2,-1/2,1/2)$, $P = (1/4,1/4,1/4)$ and $N = (0,0,1/2)$ in units of the reciprocal lattice vectors. The PDOS of both phases (c) are shown to the right in solid lines.

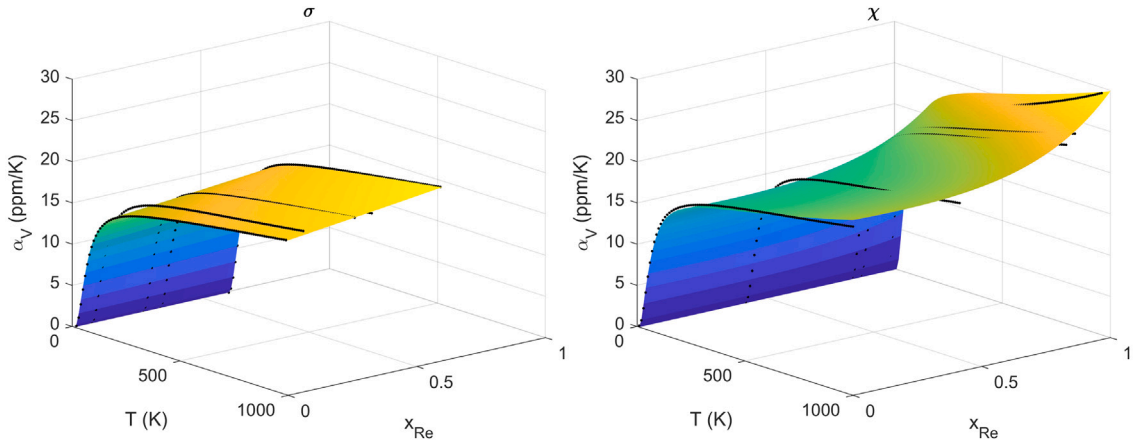

Fig. 8. The CTE of the σ and χ phase. The black dots show the result of the sublattice configurations while the surfaces show the fitted functions with parameters given in Table Table 1.

rapidly for Re concentration above 60 at.%. For the χ phase, we provide $\alpha_V(x_{Re}, T)$ for the entire Re concentration region since all sublattice configurations were dynamically stable. The non-linear increase in α_V with increasing Re content means that at 100 at.% Re the predicted CTE of χ is 1.41 times larger than a pure W structure while for σ the CTE at 60 at.% Re is only 1.11 times larger than the W structure.

4. Discussion

4.1. Modeling of the PDOS

The DG model and the QHA predict different behaviors of the CTE, in particular: the QHA predicts an increase in the CTE when the Re content is increased while, according to the DG model, the CTE is largely indifferent to changes in the Re concentration. Studies show that adding Re to bcc-W causes an increase in the CTE [29,32]. It is not unreasonable to expect similar behavior of W-Re σ and χ phases. Since the terms E_0 and F_{el} are unchanged in Eq. (3), the cause of the discrepancy lies in how the methods predict the F_{vib} term. In particular how they incorporate the PDOS. In Fig. 9 the PDOS at two different Re concentrations as well as the approximated PDOS by the DG method (dashed lines) are shown for σ and χ. The center-of-mass of the PDOS for low (□) and high (×) Re concentrations are also shown at the top of the figure. Overall, the replacement of W atoms with the slightly heavier Re atoms causes a slight softening of the phonon modes as peaks in the PDOS are shifted to lower frequencies. Such changes in the phonon spectrum will affect the behavior of α_V as the PDOS is a decisive parameter in the F_{vib} term and consequently the thermal properties [32]. In the DG model optical phonon modes are treated as acoustic [71] resulting in a parabolic-shaped approximation of the PDOS that is cut off at the Debye frequency. Despite the obvious differences between the approximated and actual PDOS structure, the DG model can often still be successful since F_{vib} depends on the integration of the PDOS [32]. However, since optical modes contribute differently to the thermal properties than acoustic [72] and the σ and χ phases contain a high number of optical modes, in this case the

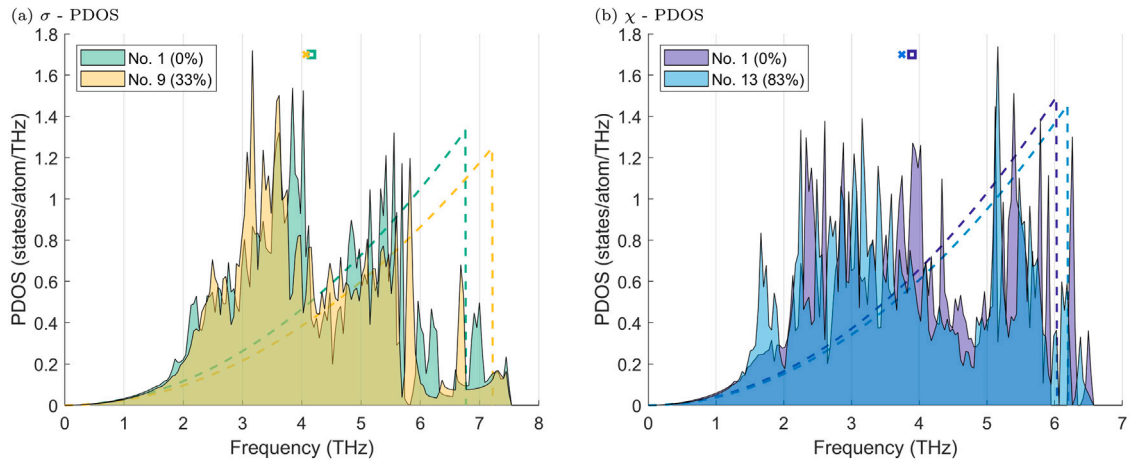

Fig. 9. Comparison of the PDOS of two (a) σ configurations and two (b) χ configurations at different Re concentrations. The dashed lines designate the approximated PDOS of the DG model.

Table 2
Average values of CTE for σ and χ in their stable Re concentration ranges compared to experimental values for bcc-W and bcc-W containing 25 at.% Re [28,29].

	α_V (ppm/K)			
T (K)	σ (45%–60% Re)	χ (70%–75% Re)	W [28]	WRe [29] (25% Re)
300	17.61	18.91	13.31	–
400	18.23	20.62	13.79	15.24
1000	20.77	23.76	14.66	16.05

approximation may lead to less precise predictions of α_V. Furthermore, the DG model does not predict a phonon softening when Re is added, instead, the Debye frequency increases with increasing Re content. This is because of the relationship between Debye temperature and the bulk modulus [33] and that the phases are predicted to stiffen with higher Re content [23,24]. In summary, in light of these approximations, there is reason to question the reliability of acoustic phonon models, such as the DG model, when applied to the σ and χ phases.

4.2. Thermal expansion mismatch

The W-based components in a fusion reactor are expected to operate under extreme temperature fluctuations and thermal gradients, often under cyclic loading. A mismatch in thermal expansion between σ and χ precipitates will contribute to the formation of thermal stresses, which can negatively affect the longevity of the component due to thermal fatigue. According to the W-Re phase diagram [20], the χ phase is thermodynamically stable at Re concentrations of about 70–75 at.% Re and the σ phase is stable at about 45–65 at.% Re with the exact range of stability depending on the temperature. From the fitted function of the thermal expansion, we can estimate the average value of α_V in the ranges for σ and χ as listed in Table 2. Experimental values of α_V for bcc-W and W-Re with 25 at.% Re content are also included in the table. If we compare α_V of bcc-W with the average values for σ and χ in their stable concentration ranges, we find a mismatch of ~32% and ~42% at 300 K, respectively, rising to ~42% and ~62% at 1000 K. Assuming the precipitates are embedded in a W-Re matrix with Re content close to the solubility limit, comparison with the experimental values of W-Re(25%) may provide a good estimation of the mismatch, which reduces to ~20% and ~35% at 400 K for σ and χ, respectively, while at 1000 K the respective mismatch increases to ~29% and ~48%.

To quantify the consequence of the mismatch in CTE, we evaluated the thermal volumetric strain, $\varepsilon_V^T = \int \alpha_V \mathrm{dT}$, when heating free-standing single-crystals from room temperature to 1000 K. For bcc-W, we obtain an ε_V^T of 1.1% while for the χ phase at its ideal composition (No. 13) the volumetric thermal strain becomes ~1.6%, which is 42% higher, indicating that the contribution of elastic energy buildup due to thermal loading may be considerable. For the ideal-composition σ phase (No. 9) a smaller deviation of a ε_V^T of 1.3% is reached. Hence, the mismatch in the CTE and ε_V^T of the χ phase is noticeably higher than the σ phase. Fig. 8 shows that this is primarily due to the χ phase being thermodynamically stable at higher Re concentrations combined with the non-linear increase in α_V. Therefore, in terms of thermal stresses originating from a mismatch in CTE, the χ precipitates are predicted to pose a higher risk than σ precipitates. It is tempting to assume that due to the difference in the stable Re content, the χ phase is less likely to form than the σ phase since irradiated W samples typically contain only a few percent Re, however, experiments indicate that this is not necessarily the case [14–16] with one early study identifying only χ type precipitates [73]. To translate the CTE and ε_V^T mismatch into stresses, which lies beyond the scope of the present work, would require detailed knowledge of, e.g., the morphology and size of the precipitates as well as the coherency and the precipitate orientation relative to the matrix. Moreover, insight into the surrounding microstructure would be necessary, as the precipitates can interact with other types of irradiation damage. A recent study by Dürrschnabel et al. [16] indicates that χ type precipitates are often located in connection with irradiation-induced voids in contrast to the σ type. The study also found that the precipitates primarily occur within "clouds" of sufficiently high transmutation product concentrations [16]. Furthermore, the interface between the precipitate and surrounding matrix may also significantly impact the CTE [74]. To attain a more complete understanding of the effects caused by the CTE mismatch, continuum mechanical modeling, using, e.g., the finite element method (FEM) with the CTE data provided in this work as input can be used.

5. Conclusions

In this paper, we have studied the CTE values of the W-Re σ and χ phases using *ab-initio* calculations. We first determined the CTE of the most stable sublattice configurations of the two phases using the DG model and the QHA. The QHA predicts an increase in CTE with increasing Re content, in line with experimental results for W-Re samples. On the contrary, the DG method predicts the Re content to have an insignificant effect. This is because the DG model predicts a small increase in the Grüneisen parameter, γ, that is largely counteracted by an increase in the bulk modulus, while the QHA predicts a larger nonlinear increase in γ when the Re content is raised. It should also be noted that the σ and χ phases contain a large number of optical modes which the DG model approximates as acoustic. Since optical and acoustic modes have different contributions to thermal expansion, this raises questions

Table A.1
Data for the σ- and χ-phases. The sublattice configuration number, No., the elements of the Wyckoff sites $klmn(o)$, the rhenium concentration, x_{Re}, the formation enthalpy H_f in units (eV/at.), and the lattice parameters a_0 and c_0 (Å) at 0 K.

σ						χ				
No.	$klmno$	x_{Re}	H_f	a_0	c_0	No.	$klmn$	x_{Re}	H_f	a_0
1	WWWWW	0.000	0.173	9.800	5.143	1	WWWW	0.000	0.288	9.873
2	ReWWWW	0.067	0.142	9.785	5.127	2	ReWWW	0.035	0.301	9.865
3	WReWWW	0.133	0.197	9.741	5.147	3	WReWW	0.138	0.322	9.839
4	ReReWWW	0.200	0.170	9.730	5.084	4	ReReWW	0.172	0.339	9.831
5	WWWWRe	0.267	0.168	9.729	5.061	5	WWReW	0.414	0.144	9.749
6	WWWReW	0.267	0.058	9.734	5.085	6	WWWRe	0.414	0.057	9.743
7	WWReWW	0.267	0.153	9.719	5.112	7	ReWReW	0.448	0.161	9.740
8	ReWWWRe	0.333	0.136	9.718	5.084	8	ReWWRe	0.448	0.064	9.736
9	ReWWReW	0.333	0.028	9.726	5.061	9	WReReW	0.552	0.211	9.719
10	ReWReWW	0.333	0.121	9.708	5.094	10	WReWRe	0.552	0.094	9.713
11	WReWWRe	0.400	0.179	9.670	5.112	11	ReReReW	0.586	0.233	9.710
12	WReWReW	0.400	0.079	9.697	5.072	12	ReReWRe	0.586	0.109	9.706
13	WReReWW	0.400	0.180	9.674	5.105	13	WWReRe	0.828	−0.008	9.626
14	ReReWWRe	0.467	0.155	9.660	5.093	14	ReWReRe	0.862	0.002	9.619
15	ReReWReW	0.467	0.052	9.682	5.056	15	WReReRe	0.966	0.036	9.595
16	ReReReWW	0.467	0.151	9.664	5.087	16	ReReReRe	1.000	0.050	9.589
17	WWWReRe	0.533	0.060	9.677	5.034					
18	WWReWRe	0.533	0.145	9.654	5.076					
19	WWReReW	0.533	0.068	9.667	5.042					
20	ReWWReRe	0.600	0.037	9.666	5.014					
21	ReWReWRe	0.600	0.116	9.648	5.053					
22	ReWReReW	0.600	0.040	9.658	5.021					
23	WReWReRe	0.667	0.076	9.636	5.029					
24	WReReWRe	0.667	0.171	9.596	5.085					
25	WReReRew	0.667	0.098	9.627	5.033					
26	ReReWReRe	0.733	0.057	9.622	5.012					
27	ReReReWRe	0.733	0.147	9.588	5.065					
28	ReReReReW	0.733	0.074	9.609	5.020					
29	WWReReRe	0.800	0.085	9.595	5.014					
30	ReWReReRe	0.867	0.067	9.589	4.991					
31	WReReReRe	0.933	0.114	9.544	5.022					
32	ReReReReRe	1.000	0.096	9.536	4.995					

Table A.2
Bulk modulus at 0 K (GPa) and Varshni parameters s (GPa) and t (K) as obtained by the QHA and the DG model for selected σ and χ configurations. The numbering refers to the configurations in Table A.1.

		QHA			DG		
		B_0	s	t	B_0	s	t
σ	No 1	294.1	6.227	208.6	294.9	2.316	129.8
	No 2	299.6	5.667	182.8	300.5	1.890	104.9
	No 6	316.1	5.154	160.7	317.0	2.096	118.3
	No 9	321.9	5.741	168.5	322.8	2.055	112.7
	No 20	337.6	5.880	161.5	348.5	2.932	145.1
χ	No 1	285.5	4.515	132.1	286.6	0.887	55.08
	No 6	324.6	5.361	151.1	325.7	1.818	98.52
	No 13	354.4	8.642	159.1	355.8	1.931	92.50
	No 14	355.6	7.397	137.2	357.0	1.911	91.45
	No 15	359.8	15.12	190.7	361.6	1.928	90.09

about the reliability of the DG model when applied to these two phases. We used the CTEs as obtained by the QHA of the selected sublattice configurations to fit an analytical function of the thermal expansion as a function of temperature and Re content: $\alpha_V(x_{Re}, T)$. An exponential dependency on the Re concentration and adopting an equation of state developed for W for the dependency of T was applied and provided a good fit with low values of RMSE. The σ configurations of high Re content were determined to be dynamically unstable and therefore our function $\alpha_V(x_{Re}, T)$ for σ is only obtained for Re concentrations below 60 at.%. In terms of mismatch in CTE, an important variable due to its influence on thermal stresses, both precipitates show high values of mismatch at the 1000 K when phases at stable Re concentrations are compared to bcc-W. When the Re content in the surrounding bcc matrix is increased the mismatch is reduced, however, it remains high, at just below 50%, for the χ phase at high temperatures. Therefore, based on our results, χ-type precipitates are expected to be a more crucial source of thermal stresses than the σ-type. This is due to the χ phases being stable at higher Re concentrations and that the CTE is predicted to increase in a non-linear fashion with the Re content.

CRediT authorship contribution statement

Anders Vesti: Writing – review & editing, Writing – original draft, Visualization, Methodology, Investigation, Formal analysis, Data curation, Conceptualization. **Denis Music:** Writing – review & editing, Methodology. **Pär A.T. Olsson:** Writing – review & editing, Supervision, Methodology, Funding acquisition, Conceptualization.

Declaration of competing interest

The authors declare that they have no known competing financial interests or personal relationships that could have appeared to influence the work reported in this paper.

Data availability

Data will be made available on request.

Acknowledgments

The authors gratefully acknowledge funding from the Swedish Research Council (grant agreement s No. 2016-04162, 2018-04348 and 2022–04497). D. Music acknowledges the financial support from the Olle Engkvist Foundation (project number 217-0023). The computations were enabled by resources provided by the National Academic Infrastructure for Supercomputing in Sweden (NAISS) at the National Supercomputer Centre (NSC), Linköping University.

Appendix A. The σ and χ configurations

Table A.1 lists the basic parameters of each of the σ and χ configurations. The numbering (No.) is the same as in Fig. 2. Table A.2 lists the fitted parameters of the Varshni relation, Eq. (14), for the selected σ and χ configurations as estimated by the quasi-harmonic approximation (QHA) and the Debye-Grüneisen (DG) model. The numbering refers to the configurations in Table A.1.

References

[1] Y. Qian, M.R. Gilbert, L. Dezerald, D. Cereceda, Using first-principles calculations to predict the mechanical properties of transmuting Tungsten under first wall fusion power-plant conditions, J. Phys.: Condens. Matter. 33 (34) (2021) 345901.

[2] V. Philipps, Tungsten as material for plasma-facing components in fusion devices, J. Nucl. Mater. 415 (1) (2011) S2–S9.

[3] S. Krat, Y. Gasparyan, A. Pisarev, I. Bykov, M. Mayer, G. de Saint Aubin, M. Balden, C.P. Lungu, A. Widdowson, Erosion at the inner wall of JET during the discharge campaign 2011–2012 in comparison with previous campaigns, J. Nucl. Mater. 456 (2015) 106–110.

[4] R.G. Abernethy, Predicting the performance of Tungsten in a fusion environment: A literature review, Mater. Sci. Technol. 33 (2017) 388–399.

[5] T. Hirai, S. Panayotis, V. Barabash, C. Amzallag, F. Escourbiac, A. Durocher, M. Merola, J. Linke, T. Loewenhoff, G. Pintsuk, et al., Use of Tungsten material for the ITER divertor, Nucl. Mater. Energy 9 (2016) 616–622.

[6] R. Pitts, X. Bonnin, F. Escourbiac, H. Frerichs, J. Gunn, T. Hirai, A. Kukushkin, E. Kaveeva, M. Miller, D. Moulton, et al., Physics basis for the first ITER Tungsten divertor, Nucl. Mater. Energy 20 (2019) 100696.

[7] J. Fellinger, M. Richou, G. Ehrke, M. Endler, F. Kunkel, D. Naujoks, T. Kremeyer, A. Menzel-Barbara, T. Sieber, J. Lobsien, et al., Tungsten based divertor development for Wendelstein 7-X, Nucl. Mater. Energy 37 (2023) 101506.

[8] M.R. Gilbert, S.L. Dudarev, S. Zheng, L.W. Packer, J.C. Sublet, An integrated model for materials in a fusion power plant: Transmutation, gas production, and helium embrittlement under neutron irradiation, Nucl. Fusion 52 (2012) 083019.

[9] J. Linke, J. Du, T. Loewenhoff, G. Pintsuk, B. Spilker, I. Steudel, M. Wirtz, Challenges for plasma-facing components in nuclear fusion, Matter Radiat. Extremes 4 (2019) 056201.

[10] H. Bolt, V. Barabash, W. Krauss, J. Linke, R. Neu, S. Suzuki, N. Yoshida, Team, ASDEX Upgrade, Materials for the plasma-facing components of fusion reactors, J. Nucl. Mater. 329 (2004) 66–73.

[11] N. Noda, V. Philipps, R. Neu, A review of recent experiments on W and high Z materials as plasma-facing components in magnetic fusion devices, J. Nucl. Mater. 241 (1997) 227–243.

[12] S.J. Zinkle, Fusion materials science: Overview of challenges and recent progress, Phys. Plasmas 12 (5) (2005) 058101.

[13] Y. Nemoto, A. Hasegawa, M. Satou, K. Abe, Microstructural development of neutron irradiated W-Re alloys, J. Nucl. Mater. 283–287 (2000) 1144–1147.

[14] T. Tanno, M. Fukuda, S. Nogami, A. Hasegawa, Microstructure development in neutron irradiated Tungsten alloys, Mater. Trans. 52 (2011) 1447–1451.

[15] M. Fukuda, T. Tanno, S. Nogami, A. Hasegawa, Effects of Re content and fabrication process on microstructural changes and hardening in neutron irradiated Tungsten, Mater. Trans. 53 (2012) 2145–2150.

[16] M. Dürrschnabel, M. Klimenkov, U. Jäntsch, M. Rieth, H.C. Schneider, D. Terentyev, New insights into microstructure of neutron-irradiated Tungsten, Sci. Rep. 11 (7572) (2021).

[17] M.J. Lloyd, A.J. London, J. Haley, M.R. Gilbert, C. Becquart, C. Domain, E. Martinez, M. Moody, P. Bagot, D. Nguyen-Manh, D. Armstrong, Interaction of transmutation products with precipitates, dislocations and grain boundaries in neutron irradiated w, Materialia (2022) 101370.

[18] T. Suzudo, M. Yamaguchi, A. Hasegawa, Stability and mobility of rhenium and osmium in Tungsten: First principles study, Modelling Simul. Mater. Sci. Eng. 22 (2014) 075006.

[19] C.-H. Huang, L. Gharaee, Y. Zhao, P. Erhart, J. Marian, Mechanism of nucleation and incipient growth of Re clusters in irradiated W-Re alloys from kinetic Monte Carlo simulations, Phys. Rev. B 96 (9) (2017) 094108.

[20] T.B. Massalski, H. Okamoto, P. Subramanian, L. Kacprzak, W.W. Scott, Binary Alloy Phase Diagrams, vol. 1, (no. 2) American society for metals Metals Park, OH, 1986.

[21] C. Berne, M. Sluiter, Y. Kawazoe, T. Hansen, A. Pasturel, Site occupancy in the Re-W sigma phase, Phys. Rev. B 64 (2001) 144103.

[22] J.-C. Crivello, A. Breidi, J.-M. Joubert, χ And σ phases in binary rhenium–transition metal systems: a systematic first-principles investigation, Inorg. Chem. 52 (7) (2013) 3674–3686.

[23] G. Bonny, A. Bakaev, D. Terentyev, Y.A. Mastrikov, Elastic properties of the sigma W-Re phase: A first principles investigation, Scr. Mater. 128 (2017) 45–48.

[24] A. Vesti, P. Hiremath, S. Melin, P.A.T. Olsson, Ab-initio investigation of mechanical and fracture-related properties of W-Re σ and χ precipitates, J. Nucl. Mater. (2023) 154261.

[25] G. Bonny, A. Bakaev, D. Terentyev, Assessment of hardening due to non-coherent precipitates in Tungsten-rhenium alloys at the atomic scale, Sci. Rep. 9 (2019) 2045–2322.

[26] R.G. Abernethy, J.S.K.L. Gibson, A. Giannattasio, J.D. Murphy, O. Wouters, S. Bradnam, P.L. W., M.R. Gilbert, M. Klimenkov, M. Rieth, H.C. Schneider, C.D. Hardie, S.G. Roberts, D.E.J. Armstrong, Effects of neutron irradiation on the brittle to ductile transition in single crystal Tungsten, J. Nucl. Mater. 527 (2019) 151799.

[27] J. Conway, Properties of some refractory metals. III. thermal expansion characteristics of Tungsten, rhenium, tantalum, molybdenum, niobium, W-25Re, Ta-10W, and Mo-50Re, Tech. rep., General Electric Co., Cincinnati, Ohio. Nuclear Materials and Propulsion, 1965.

[28] K. Wang, R.R. Reeber, The role of defects on thermophysical properties: Thermal expansion of V, Nb, Ta, Mo and W, Mater. Sci. Eng. R 23 (3) (1998) 101–137.

[29] V. Andrianova, A.Z. Zhuk, V. Ziachenko, E.B. Zaretskii, V.A. Petukhov, V.Y. Chekhovskoi, AnomaloUS concentration dependence of some physical properties of Tungsten-rhenium alloys, High Temp. 21 (1) (1983) 70–75.

[30] V. Zaichenko, R. Mints, V. Petukhov, Thermal expansion of W-Re alloys in the solid-solution region at temperatures of 200-900 C, Teplofiz. Vys. Temp. 12 (5) (1974) 1015–1018.

[31] L. Zhou, Y. Li, Simulation study on uniaxial tensile mechanical and thermal properties of rhenium Tungsten alloys, Nucl. Instrum. Methods Phys. Res. B 535 (2023) 247–254.

[32] T. Dengg, V. Razumovskiy, L. Romaner, G. Kresse, P. Puschnig, J. Spitaler, Thermal expansion coefficient of WRe alloys from first principles, Phys. Rev. B 96 (3) (2017) 035148.

[33] P. Söderlind, L. Nordström, L. Yongming, B. Johansson, Relativistic effects on the thermal expansion of the actinide elements, Phys. Rev. B 42 (7) (1990) 4544.

[34] S. Baroni, P. Giannozzi, E. Isaev, Density-functional perturbation theory for quasi-harmonic calculations, Rev. Mineral. Geochem. 71 (1) (2010) 39–57.

[35] J.C. Crivello, J.M. Joubert, First principles calculations of the σ and χ phases in the Mo-Re and W-Re systems, J. Phys.: Condens. Matter. 22 (2009) 035402.

[36] K. Momma, F. Izumi, VESTA 3 for three-dimensional visualization of crystal, volumetric and morphology data, J. Appl. Crystallogr. 44 (6) (2011) 1272–1276.

[37] P.A.T. Olsson, A.R. Massih, J. Blomqvist, A.-M.A. Holston, C. Bjerkén, Ab initio thermodynamics of zirconium hydrides and deuterides, Comput. Mater. Sci. 86 (2014) 211–222.

[38] C. Wolverton, A. Zunger, First-principles theory of short-range order, electronic excitations, and spin polarization in Ni-V and Pd-V alloys, Phys. Rev. B 52 (12) (1995) 8813.

[39] D. Music, S. Khayyamifar, J. Hektor, Conflicting primary and secondary properties of thermoelectric devices–a case study on the thermomechanical behavior of ZrNiSn, Comput. Mater. Sci. 230 (2023) 112530.

[40] J.C. Slater, Introduction to Chemical Physics, Read Books Ltd, 2011.

[41] V. Moruzzi, J. Janak, K. Schwarz, Calculated thermal properties of metals, Phys. Rev. B 37 (2) (1988) 790.

[42] F. Birch, Finite strain isotherm and velocities for single-crystal and polycrystalline NaCl at high pressures and 300 K, J. Geophys. Res.: Solid Earth 83 (B3) (1978) 1257–1268.

[43] Curve Fitting Toolbox : for Use With MATLAB® : User's Guide, Version 1, MathWorks, Natick, MA, 2001.

[44] N.V. Kozyrev, V.V. Gordeev, Thermodynamic properties and equation of state for Tungsten, Crystals 13 (10) (2023) 1470.

[45] G. Kresse, J. Hafner, Ab initio molecular dynamics for liquid metals, Phys. Rev. B 47 (1) (1993) 558.

[46] G. Kresse, J. Furthmüller, Efficiency of ab-initio total energy calculations for metals and semiconductors using a plane-wave basis set, Comput. Mater. Sci. 6 (1) (1996) 15–50.

[47] G. Kresse, D. Joubert, From ultrasoft pseudopotentials to the projector augmented-wave method, Phys. Rev. B 59 (1999) 1758–1775.

[48] P.E. Blöchl, Projector augmented-wave method, Phys. Rev. B 50 (1994) 17953–17979.

[49] J.P. Perdew, K. Burke, M. Ernzerhof, Generalized gradient approximation made simple, Phys. Rev. Lett. 77 (1996) 3865–3868.

[50] M. Methfessel, A. Paxton, High-precision sampling for Brillouin-zone integration in metals, Phys. Rev. B 40 (6) (1989) 3616.

[51] H.J. Monkhorst, J.D. Pack, Special points for Brillouin-zone integrations, Phys. Rev. B 13 (12) (1976) 5188.

[52] P. Pulay, Convergence acceleration of iterative sequences. The case of SCF iteration, Chem. Phys. Lett. 73 (2) (1980) 393–398.

[53] W.P. Davey, The lattice parameter and density of pure Tungsten, Phys. Rev. 26 (1925) 736–738.

[54] L.-G. Liu, T. Takahashi, W.A. Bassett, Effect of pressure and temperature on the lattice parameters of rhenium, J. Phys. Chem. Solids 31 (6) (1970) 1345–1351.

[55] A. Togo, L. Chaput, T. Tadano, I. Tanaka, Implementation strategies in phonopy and phono3py, J. Phys.: Condens. Matter. 35 (35) (2023) 353001, http://dx.doi.org/10.1088/1361-648X/acd831.

[56] A. Togo, First-principles Phonon calculations with Phonopy and Phono3py, J. Phys. Soc. Japan 92 (1) (2023) 012001, http://dx.doi.org/10.7566/JPSJ.92.012001.

[57] A. Togo, L. Chaput, I. Tanaka, G. Hug, First-principles phonon calculations of thermal expansion in Ti_3SiC_2, Ti_3AlC_2, and Ti_3GeC_2, Phys. Rev. B 81 (2010) 174301.
[58] L. Chaput, A. Togo, I. Tanaka, G. Hug, Phonon-phonon interactions in transition metals, Phys. Rev. B 84 (9) (2011) 094302.
[59] K. Parlinski, Z. Li, Y. Kawazoe, First-principles determination of the soft mode in cubic ZrO_2, Phys. Rev. Lett. 78 (21) (1997) 4063.
[60] W. Setyawan, N. Gao, R.J. Kurtz, A Tungsten-rhenium interatomic potential for point defect studies, J. Appl. Phys. 123 (2018) 205102.
[61] N. Soga, Comparison of measured and predicted bulk moduli of tantalum and Tungsten at high temperatures, J. Appl. Phys. 37 (9) (1966) 3416–3420.
[62] F.H. Featherston, J. Neighbours, Elastic constants of tantalum, Tungsten, and molybdenum, Phys. Rev. 130 (4) (1963) 1324.
[63] E. Fisher, D. Dever, Temperature dependence of elastic moduli of ruthenium, rhenium, cobalt, dysprosium, and erbium a study of the elastic anisotropy-phase transformation relationship, Tech. rep., Argonne National Lab., Ill., 1967.
[64] P. Söderlind, B. Johansson, Calculated thermal expansion of d and f transition metals, Thermochimica acta 218 (1993) 145–153.
[65] M.H. Manghnani, K. Katahara, E.S. Fisher, Ultrasonic equation of state of rhenium, Phys. Rev. B 9 (4) (1974) 1421.
[66] X.-G. Lu, M. Selleby, B. Sundman, Theoretical modeling of molar volume and thermal expansion, Acta Mater. 53 (8) (2005) 2259–2272.
[67] P.A.T. Olsson, First principles investigation of the finite temperature dependence of the elastic constants of zirconium, magnesium and gold, Comput. Mater. Sci. 99 (2015) 361–372.
[68] Y. Varshni, Temperature dependence of the elastic constants, Phys. Rev. B 2 (10) (1970) 3952.
[69] V. Drebushchak, Thermal expansion of solids: Review on theories, J. Therm. Anal. Calorim. 142 (2) (2020) 1097–1113.
[70] M. Palumbo, A. Dal Corso, Lattice dynamics and thermophysical properties of hcp Os and Ru from the quasi-harmonic approximation, J. Phys.: Condens. Matter. 29 (39) (2017) 395401.
[71] A. Otero-de-la Roza, D. Abbasi-Pérez, V. Luaña, Gibbs2: A new version of the quasiharmonic model code. II. Models for solid-state thermodynamics, features and implementation, Comput. Phys. Comm. 182 (10) (2011) 2232–2248.
[72] C.-R. Xu, L. Shao, N. Ding, H.-H. Jiang, B.-Y. Tang, Study of thermal properties of TiCN by Debye Einstein model, Debye Grüneisen model and quasiharmonic approximation, Physica B 674 (2024) 415589.
[73] R. Williams, F. Wiffen, J. Bentley, J. Stiegler, Irradiation induced precipitation in Tungsten based, W-Re alloys, Metall. Trans. A 14 (1983) 655–666.
[74] P.A.T. Olsson, I. Awala, J. Holmberg-Kasa, A.M. Krause, M. Tidefelt, O. Vigstrand, D. Music, Grain size-dependent thermal expansion of nanocrystalline metals, Materials 16 (14) (2023) 5032.